Neutralization of hyperthermal multiply charged ions at surfaces: Comparison between the extended dynamical overbarrier model and experiment

J. Ducrée and H. J. Andrä
Institut für Kernphysik, Westfälische Wilhelms Universität Münster, Wilhelm-Klemm-Strasse 9, D-48149 Münster, Germany

U. Thumm*
J. R. Macdonald Laboratory, Department of Physics, Kansas State University, Manhattan, Kansas 66506-2604
(Received 22 March 1999)

Within a semiclassical model, we investigate the dynamic neutralization and relaxation of slow ($E_{\mathrm{kin}} < 100$ eV) multiply charged ions which are reflected on metal surfaces. Special emphasis is devoted to near-surface interaction mechanisms. Our model includes a Monte Carlo sampling over projectile parameters and detailed ionic structure calculations of projectile energy levels. In a full trajectory simulation, our results *simultaneously* comply with measured trends in projectile kinetic energy gains and final charge-state distributions of the reflected ions as well as total electron yields and spectra. Recently discovered characteristic features in the electron spectra can be uniquely assigned to distinct above-surface regions of the projectile trajectory. [S1050-2947(99)03009-7]

PACS number(s): 34.50.Dy, 34.70.+e, 79.20.Rf

I. INTRODUCTION

In slow collisions with complex targets, multiply charged ions (MCI's) capture many electrons into excited states, thereby forming unstable, multiply excited projectiles which are commonly referred to as ''hollow ions.'' These hollow ions partly relax by emitting Auger electrons and, to a smaller extent, photons, and get destroyed in close encounters with the target. Over the past decade, both the formation and decay of hollow ions have been a subject of numerous experimental and theoretical investigations. These studies used a variety of targets, such as large atoms [1–4], clusters [5–8], and metal [9–16] or insulator [17–24] surfaces. Benefiting from this comprehensive collection of experimental data and theoretical work, the knowledge in this field has made rapid progress in the past decade [25].

At present, the most important mechanisms of ion neutralization and relaxation have been identified and assigned to distinguished interaction zones. Typically, at 20 to 30 atomic units (a.u.) in front of the surface, the potential barrier between the ion and the target drops below the target Fermi level, triggering the onset of efficient neutralization via resonant electron capture (RC), which prevails the competing resonant loss (RL) in the inverse direction.

Close to the surface, projectiles are reflected or they penetrate into the bulk region depending upon the beam energy and its angle of incidence. Several experiments have been designed to investigate processes taking place above and below the surface [15,16,26–33]. These measurements analyze emitted-electron [10,11] and x-ray yields [34–37], as well as the final charge-state distributions [11,38], the projectile energy loss [13,39,40], and the angular deflection of the projectile [18,41,42].

With the work of Burgdörfer *et al.* [9], a semiclassical description of the projectile neutralization, the so-called classical overbarrier model (COM), became available which is able to reproduce measured image energy gains of the incoming projectiles. Owing to the intricate interaction dynamics involved, more sophisticated descriptions can presently deal with only selected aspects of the scattering process, and a full quantum-mechanical treatment of the complete course of interaction is still out of reach.

The present work employs a refined and extended version of the COM to simulate projectile energy gains, final charge-state distributions, and the emission of projectile Auger electrons along a whole reflection trajectory. In Sec. II, we describe the basic ingredients of our simulation. Based on our findings combined with the recently discovered signatures of metastable electrons in the *K*-Auger spectra [43], an interaction model is worked out in Sec. III. Section IV presents the calculated results which are compared to different experiments. In Sec. V, the variation of several simulation parameters is discussed. Finally, in Sec. VI, we summarize our results. Throughout this paper, we use atomic units ($e = m_e = \hbar = 1$), unless stated otherwise.

II. OUTLINE OF THE SIMULATION MODEL

Our calculations are based on the ''standard'' COM for above-surface charge exchange between incident MCI's and metal surfaces [9,23]. This model has been refined in the past by improved screening models [12,44] and adapted to collisions with insulators [22,23]. These modified COM versions have been shown to provide good estimates for measurable quantities, e.g., total electron yields [15], above- and near-surface Auger emission [15,16,43], and final charge-state distributions [44]. However, this success has been achieved mostly by concentrating on *one* particular observable for a distinct collision system. In the present simulation, which focuses on metal surfaces and hyperthermal incident energies $E_{\mathrm{kin}} < 100$ eV, we will eliminate this severe restriction.

*Corresponding author. Electronic address: thumm@phys.ksu.edu

The simulation begins near the first capture distance R_{crit}, is continued through the vertex region, and ends when the neutralized MCI has receded so far from the surface that further exchange becomes impossible. For this full trajectory, a model covering all interaction regions, in particular the region near the vertex, is required. However, the validity of the standard COM becomes questionable when the projectile approaches the first bulk layer to within a few atomic units. On the other hand, mechanisms taking place deep inside the bulk electron have been studied in detail [45,46]. The lack of a sophisticated *a priori* treatment for the complicated near-surface interaction zone has therefore led us to smoothly interpolate between the long-distance and the subsurface domains. The modeling of this interface region will prove to be of crucial importance for the outcome of our simulation. In contrast to previous approaches which considered only a two-shell projectile and static interaction rates along the MCI path [16], the present model, referred to as ''extended dynamical COM (EDCOM),'' includes all projectile levels for the relevant interactions.

As a further extension to the standard COM, we include detailed atomic structure calculations, a Monte Carlo sampling, and we allow for arbitrary incident angles, covering normal and grazing incidence. In this manner we are able to explain structures and intensities in autoionization spectra, such as, e.g., the exclusive occurrence of the so-called KLV_W peak and KL_1L_1 shoulder [43] in the spectra of metastable He-like projectiles in $(1s2s)$ configurations (Sec. IV E 1 below). Other quantities, such as energy gains and secondary electron yields, which have already been modeled successfully, are monitored to agree with the experimental data to a reasonable extent (Sec. IV A and IV C below).

In what follows, we refer to R as the distance of the projectile nucleus perpendicular to the first bulk layer at $R=0$. Values for the jellium edge located at z_j and the image plane at z_{im} are taken from Ref. [47]. The distinction between the $(R=0)$ and the z_j plane is important for the simulation of spectra originating from reflected MCI beams [16].

A. Atomic energy levels

In the present work we significantly improved the modeling of autoionization by integrating the calculation of binding energies (at the Hartree-Fock level) into our simulation. For any projectile configuration vector $\{a_n\}$ occurring along the course of the ion-surface interaction (a_n designates the number of electrons in projectile shell n), we employ the Cowan code [48] to generate the corresponding average total configuration binding energies of the undistorted projectile ion $\varepsilon_{\mathrm{tot}}^{\infty}(\{a_n\})$ and each of its shells $\{\varepsilon_n^{\infty}(\{a_n\})\}$. For the moderate charge states considered in this work, it is sufficient to keep track of the shells $n=1,\ldots,10$ since no higher-lying levels are involved in the interaction dynamics. The 10-dimensional vectors are stored to accelerate the evaluation of recurring configurations.

In general, we do not resolve the populations in particular projectile subshells. For the L shell, however, we calculate the $2s$ and $2p$ binding energies and keep track of the respective subshell populations. We assume that the $2p$ level is preferentially populated via Auger ionization (AI) and side-feeding processes, as suggested by its higher degeneracy and its lower binding energy. With increasing occupation, L-shell relaxation via *LLM* Coster-Kronig (CK) and *LLL* super-CK (sCK) transitions becomes energetically possible and proceeds by one and two orders of magnitude faster, respectively, than other Auger processes [10].

The so-evaluated vector of asymptotic configuration energies $\varepsilon_n^{\infty}(\{a_n\})$ relates to hydrogenic radii $\langle r\rangle_n = n/\sqrt{|2\varepsilon_n^{\infty}|}$. Both ε_n^{∞} and $\langle r\rangle_n$ decisively affect the course of interaction, which is governed by RC, RL, ''peeling off (PO),'' ''side feeding (SF),'' and ''continuum promotion (CP)'' of electrons, and therefore determine the shape of the simulated Auger spectra. (A detailed discussion of PO, SF, and CP processes will follow in Sec. II D 1, II D 2, and II E below.)

B. Auger autoionization rates

In order to explain particular features in emitted electron spectra, such as the sharp and tiny KLV_W peak and the KL_1L_1 shoulder [43,33], we have to take a closer look at the sequence of projectile autoionization steps on the incoming trajectory. Vaeck and Hansen [49] have shown that typical lifetimes of hollow N^{q+} ions critically depend on the difference of the quantum numbers between neighboring atomic shells. As a rule of thumb, Auger processes producing the smallest energies of the free electron possess the fastest rates [50]. As a consequence for our simulation, decay channels with the smallest change in the principal quantum number n and with no variation in the angular momentum quantum number l are favored over channels with larger Δn and Δl. As long as Rydberg levels host the majority of captured electrons, sCK transitions with $\Delta n=0$ and CK transitions with $\Delta n=1$ are suppressed because the potential energy gain due to the vacancy filling is insufficient to eject an electron above the vacuum threshold.

In our original COM program [23], we had used autoionization rates that were obtained as an analytical fit to Hartree-Fock ionic structure calculations based on the Cowan code [9,48],

$$\Gamma^{\mathrm{AI}}_{n_{\mathrm{ini}},n_{\mathrm{fin}}} = \frac{5.06\times 10^{-3}}{(n_{\mathrm{ini}}-n_{\mathrm{fin}})^{3.46}}. \tag{1}$$

These are still used in the EDCOM for all transitions other than *KLL* Auger processes.

KLL rates for nitrogen ions are now taken from [51] where these values are tabulated for all $1s2s^x2p^y$ configurations of $(6-x-y)$-ionized nitrogen. For other projectiles (of nuclear charge q_{nuc}), we use the same *KLL* rates, except that the values are interpolated for an effective L population $a_n' = 6a_n/q_{\mathrm{nuc}}-1$. In this way, the *KLL* rates for maximum L-shell population, $a_L = q_{\mathrm{nuc}}-1$, around the $1s$ core coincide for all projectiles. We also employ constant *KLM* rates $\Gamma^{\mathrm{KLM}}=5.06\times 10^{-5}$.

Since good estimates for the KLV_W rates are not known, the ratio between K Auger and KLV_W intensities is not well represented. Due to this lack of data, we adopted Eq. (1) for AI and accounted for the nonequivalence of the two electron states in the L shell and the V_W shell n_W by scaling $\Delta n = n_W-2$ with a factor of 1.5 and the overall rate with 0.25, i.e.,

$$\Gamma_n^{KLV_W} = 0.25 \times 5.06 \times 10^{-3} / (1.5 \Delta n)^{3.46}. \quad (2)$$

For $n_W \geq 4$, these rates are of the order of 2.8×10^{-5} and thus about two orders of magnitude slower than the fastest AI transitions. This velocity ratio corresponds to the experimentally observed intensity of the KLV_W peak, which amounts to about 1% of the total *K*-Auger intensity [43]. In view of the much faster processes governing the evolution of projectile level occupations [cf. Eq. (10) below], the impact of KLV_W transitions on the overall interaction dynamics is negligible. However, by implementing KLV_W processes in the ED-COM, we will be able to reproduce the measured KLV_W peak positions in a dynamic simulation. As a characteristic signature of the above-surface dynamics of the hyperthermal ion-surface collisions investigated by our semiclassical interaction model, the verification of the KLV_W peak energy poses a crucial test for our simulation.

We also include LLM-CK and LLL-sCK processes with fixed rates $\Gamma^{\mathrm{CK}} = 0.05$ and $\Gamma^{\mathrm{sCK}} = 1.0$, respectively, in the simulation. Accordingly, CK transitions are about one order of magnitude faster than the autoionization rates specified in Eq. (1) and sCK processes proceed almost instantaneously with respect to the other rates. However, CK and especially sCK processes are inhibited if the transition energy does not lead to emission above the continuum threshold. Both processes basically redistribute the *L*-shell population from the preferentially populated $2p$ level into the $2s$ level. The existence of an intense KL_1L_1 component in measured autoionization spectra [43,10,16] provides strong evidence for this *L*-shell relaxation channel. We shall return to a detailed discussion of *K*-Auger electron emission in Sec. IV.

C. Resonant charge transfer

In the model of Burgdörfer *et al.* [9], charge transfer is described in terms of a *continuous* current of electronic charge over the potential barrier formed by the effective potential

$$V_{\mathrm{eff}}(z,R) = V_{\mathrm{proj}}(q, z-R) + V_{\mathrm{im},p}(q, z+R) + V_{\mathrm{im},e}(z) \quad (3)$$

governing the motion of an active electron in the field of the projectile and a conducting surface. The contributions to V_{eff} are the projectile Coulomb potential V_{proj}, the image potential of the projectile (considered as a point charge $-q$) $V_{\mathrm{im},p}$, and the self-image potential of the active electron $V_{\mathrm{im},e}$. These potentials depend on the electronic coordinate perpendicular to the surface along an axis through the projectile nucleus, *z*, and, parametrically, on *R*.

In modeling the resonant transfer processes, we follow [9,23]. The resonant capture rate

$$\Gamma_n^{\mathrm{RC}}(R) = \sigma(R) j_n(R),$$
$$j_n(R) = \frac{1}{4} \int_{\max(V_b, \varepsilon_{n-1/2})}^{\min(-W, \varepsilon_{n+1/2})} dE D(E) \sqrt{2(E - V_b)} \quad (4)$$

is given by the product of the current density j_n and the minimum geometrical cross section $\sigma(R)$ of the area through which classically allowed electron transfer across the potential barrier (of height V_b situated between the projectile at *R* and the surface) is possible. This area is parallel to the surface at the distance z_b given by the condition $-W = V_{\mathrm{eff}}(z_b, R)$. $D(E) = \sqrt{2}/\pi^2 \sqrt{E - V_0}$ represents the electronic density of valence-band states per unit volume in an ideal free-electron-gas metal.

Resonant loss from occupied ionic levels into empty band states is quantified by

$$\Gamma_n^{\mathrm{RL}}(R) = \nu_n P(\varepsilon_n) \Theta(W + \varepsilon_n(R))$$
$$\nu_n = \frac{q_{\mathrm{eff},n}^2}{2\pi n^3}. \quad (5)$$

The RL mechanism is driven by the frequency ν_n of an electron in an atomic orbit with $\varepsilon_n(R) > -W$ and the probability $P(\varepsilon_n)$ for a random orbit to hit the saddle.

In contrast to our previous COM version [23], the ED-COM employs a ''truly resonant'' charge transfer, where resonance requires the initial binding energy of the target level to coincide with the binding energy of the projectile level *after* capture. In comparison with our previous COM version, this means that projectile levels are shifted upwards such that deeper-lying levels are more likely to be populated via RC due to the additional intra-atomic screening by formerly captured electrons.

D. Interactions near the surface

Interactions within the near-surface zone are strongly influenced by the target band electrons pouring into the Coulomb well around the projectile core. The most prominent near-surface interaction mechanisms are the direct transfer of electrons from target states into inner shells of the MCI (SF) [44,45,52,53] and the loss of loosely bound projectile electrons due to additional screening enforced by the tightly packed induced charge cloud (PO) [9,54].

1. Side feeding

For incident ion energies of up to several hundred keV and for a wide range of initial ion charge states and target materials, experiments on the final charge distribution of reflected projectiles reveal that the vast majority of MCI's emerges in a neutral charge state [11,55,56]. It is also well known that a mere above-surface autoionization cascade faces the ''bottle-neck problem,'' i.e., the interaction time on the incoming path falls below the overall projectile relaxation time. Therefore, it has been suggested that tightly bound projectile levels may predominantly be filled with valence-band electrons in a region of strong overlap with the target electron distribution [16,38,44,52,57,58]. The short passage time through this region and the high degrees of inner-shell occupation which have been identified by means of high-resolution Auger spectroscopy [16,32,33] imply filling rates for SF processes that lie about one order of magnitude above the fastest intra-atomic Auger rates.

We introduce such an additional inner-shell population mechanism on the basis of *XCC*-like processes ($X \in \{K, L, M, \ldots\}$). These two-electron processes are similar to regular Auger processes. However, the participating two electrons initially belong to the induced valence-band charge cloud (*C*) surrounding the projectile ionic core near and be-

low the surface. *LCC* rates Γ_L^{SF} have been approximated by *LCV* processes [45] where a charge cloud electron (*C*) fills the *L* vacancy while exciting a plasmon or an electron-hole pair in the valence band (*V*). Since *C* electrons remain localized around the ionic core, approximate *XCC* rates Γ_n^{SF} can be derived in analogy to ordinary intra-atomic Auger rates [59].

For all collision systems and all localized atomic levels $1 \leqslant n \leqslant n_{\mathrm{loc}}$, we assume a single base rate $\Gamma_0^{\mathrm{SF}} = 0.01$. In our dynamic simulation, we found that the *LCV* rates specified in [45] for N embedded into Al are too slow to explain measured final charge-state distributions of reflected projectiles. In [16], simulations and experiments have been conducted for N^{6+} projectiles impinging on gold targets where, in order to reproduce the measured data, a constant *LCV* base rate according to [45] has been used along the whole ion trajectory. However, the calculated *LCV* rates for Au [45] exceed the rates on Al by a factor of ≈ 4, which appears to be in contradiction to the similarity of the observed *K*-Auger spectra, in particular, regarding the high degree of inner-shell filling at the time of *K*-Auger decay observed for both target surfaces [16,33]. The sensitivity of observable results on Γ_0^{SF} will be discussed in Sec. V below.

For each shell *n*, Γ_0^{SF} is multiplied by the charge of the induced charge cloud, $-q$, balancing the core charge *q*, and by the number of *n*-shell vacancies N_n^{vac}. Accounting for the strong $(1/\Delta n)^{3.46}$ scaling of Auger rates $\Gamma_{n',n}^{\mathrm{AI}}$ with the difference Δn between participating levels [9] [Eq. (1)], we apply another Δn-dependent factor for the Auger-like SF process. This factor rapidly decreases from the most loosely bound localized level n_{loc} and becomes unity for the *L* shell. This way, the base rate Γ_0^{SF} can be compared to the *LCV* rates which have been calculated for various ion and target species [45]. We arrive at the side-feeding rate

$$\Gamma_n^{\mathrm{SF}}(R) = \Gamma_0^{\mathrm{SF}} q N_n^{\mathrm{vac}} N_n^{\mathrm{ol}}(R) \left(\frac{n_{\mathrm{loc}} + 1 - n_L}{n_{\mathrm{loc}} + 1 - n} \right)^{3.46}, \qquad (6)$$

$$N_n^{\mathrm{ol}}(R) = \begin{cases} \dfrac{V_n^{\mathrm{ol}}(R)}{V_n} & \text{if } R > z_j - \langle r \rangle_n \\ 1 & \text{otherwise} \end{cases} \qquad (7)$$

for each projectile shell *n*. The spatial variation of Γ_n^{SF} is represented by the factor $N_n^{\mathrm{ol}}(R)$. It is expressed in terms of the quotient of the orbital volume V_n^{ol} overlapping with the metal electron distribution and its undisturbed orbital volume $V_n = 4\pi/3\langle r \rangle_n^3$. If the projectile has penetrated the jellium edge by more than the orbital radius $\langle r \rangle_n$, we assume $N_n^{\mathrm{ol}}(R)$ to remain constant at the value 1. $N_n^{\mathrm{ol}}(R)$ obviously vanishes for distances $R > \langle r \rangle_n + z_j$. For the small impact energies far below 100 eV studied in this work, no velocity dependence of the SF rate is taken into account.

The assumption of a fixed and planar jellium edge at z_j is certainly a crude simplification. An ionic core near the surface significantly disturbs the electronic surface potential and attracts valence-band electrons. Within the present model, this effect could be represented by a shift of z_j towards the projectile nucleus. Within the overall accuracy of our approach, however, we may neglect this effect.

2. Peeling off

With the onset of charge transfer at R_{crit}, mainly outer ionic levels are populated. These Rydberg orbitals with typical radii $\langle r \rangle_n \simeq R_{\mathrm{crit}}$ are increasingly disturbed as the MCI approaches the bulk. In contrast to previously implemented *instantaneous* PO mechanisms which become effective at the moment when the MCI enters the bulk region [15,54], we examine the influence of a *dynamic* PO on the speed of electron transport from Rydberg states into inner levels along the whole interaction phase.

By testing various PO model rates, it became evident that a mere geometric criterion triggering the instantaneous loss of an electron as soon as a certain fraction of the MCI orbital volume overlaps with the bulk jellium has to fail. For the case of instantaneous loss, we observed that levels which are replenished by RC may immediately be lost due to peel-off. This leads to simulation results for the final charge-state distributions of the projectile in disagreement with experiment [11,40,55].

Our modeling for PO smoothly interpolates between the remote region and the bulk limit. We assume that near the surface, for $R < \langle r \rangle_n + z_j - \lambda_{\mathrm{scr}}$, when the electron has ''lost touch'' with the ionic core due to screening, the outermost orbital is likely to move to the valence-band continuum if its radius $\langle r \rangle_n$ exceeds the screening length λ_{scr}. This model assumes that the occupied orbitals are either spherically symmetric or oriented towards the surface. This assumption complies with the RC mechanism, which requires a certain overlap between atomic orbitals and band states.

Guided by the derivation of the resonant loss rate in [9], we arrive at the PO rate

$$\Gamma_n^{\mathrm{PO}}(R) = a_n \frac{N_n^{\mathrm{ol}}(R)}{T_n} \frac{2\pi \langle r \rangle_n}{L_n(R)} \Theta(\langle r \rangle_n - \lambda_{\mathrm{scr}}(R)), \qquad (8)$$

which is composed of several constituents. The base rate is given by the inverse orbiting time T_n of an electron in an unperturbed orbital. As in Eq. (6), we reduce T_n by a volume factor $N_n^{\mathrm{ol}}(R)$.

The term $L_n(R)/(2\pi \langle r \rangle_n)$ corrects T_n to yield the ''reaction time'' for an atomic electron. We assume that an electron which is captured at $R - z_j = \langle r \rangle_n$ and enters an atomic orbital does not get perturbed by the target electron gas until it has covered the distance $L_n(R)$. This period decreases with the ratio of the vacuum section $L_n(R)$ of the classical orbital above z_j and its circumference $2\pi \langle r \rangle_n$. The unit step function Θ in Eq. (8) disables PO for levels with radii $\langle r \rangle_n$ smaller than the screening length $\lambda_{\mathrm{scr}}(R)$.

We model the screening length in Eq. (8),

$$\lambda_{\mathrm{scr}}(R) = \lambda_{\mathrm{scr}}^0 \left(\frac{\max(R,0)}{z_j} + 1 \right), \qquad (9)$$

to reach its bulk value λ_{scr}^0 at $R = 0$. Above the first bulk layer, $\lambda_{\mathrm{scr}}(R)$ increases linearly in *R* and equals $2\lambda_{\mathrm{scr}}^0$ at the jellium edge $R = z_j$. Due to the nonlinear response of the surface electron distribution to the nearby MCI, the linear scaling in *R*, the neglect of a variation with *q*, and the particular choice of the slope, Eq. (8) can represent only a crude estimate for the dependence of λ_{scr} on q, n, and *R*.

We note that the introduction of PO in addition to the RL channel is motivated by mere technical reasons. In a precise theory, both effects could not be distinguished and represent resonant electron flow into empty band states in the spirit of the model underlying RL. However, the artificial distinction between these two electron loss mechanisms in the EDCOM is essential since the calculation of ionic level binding energies described in Sec. II A is incomplete. Ionic levels are not only subject to shifts by the image potential leading to RL. While the MCI approaches the surface, levels are also increasingly elevated by the screening of the induced charge cloud which eventually strips off loosely bound outer shell electrons. The evaluation of these additional level shifts in the highly inhomogeneous region shortly above the surface is far beyond the scope of the present theory. In order to account for this electron loss mechanism (referred to as PO) in a quantitative manner, we therefore employ simple geometric arguments.

E. Continuum promotion

Due to the action of the repulsive projectile image potential $V_{\mathrm{im},p}$ and the mutual screening of projectile electrons, atomic levels are shifted upwards with respect to their asymptotic values ε_n^∞ as the MCI approaches the surface. As the orbital energies $\varepsilon_n=\varepsilon_n^\infty+I_{\mathrm{im},p}$ reach the ionization threshold, electrons in shell n are detached from the projectile, i.e., promoted to the continuum. For the low projectile velocities considered in this work, we assume immediate electron loss due to CP as soon as $\varepsilon_n>0$.

F. Evolution of projectile level populations

For MCI–metal-surface collisions, we obtain the dynamically varying populations a_n of projectile shells with principal quantum number n as solutions of the system of rate equations of the form [23]

$$\begin{aligned}\frac{da_n}{dt}=&\theta(A_n-a_n)\Gamma_n^{\mathrm{RC}}-a_n\Gamma_n^{\mathrm{RL}}\\&+w_n^{\mathrm{fin}}\sum_{n'>n}\Gamma_{n',n}^{\mathrm{AI}}w_{n'}^{\mathrm{ini}}-2w_n^{\mathrm{ini}}\sum_{n'<n}\Gamma_{n,n'}^{\mathrm{AI}}w_{n'}^{\mathrm{fin}}\\&+\theta(A_n-a_n)\Gamma_n^{\mathrm{SF}}-a_n\Gamma_n^{\mathrm{PO}}-\theta(n-4)a_n\Gamma_n^{KLV_W}\\&-\delta_{n,M}\Gamma^{\mathrm{CK}}-\delta_{n,L}\Gamma^{\mathrm{sCK}}\\&+(\delta_{n,K}-\delta_{n,L}-\delta_{n,M})a_La_M\Gamma^{KLM}.\end{aligned}\tag{10}$$

The ''traditional'' COM developed by Burgdörfer *et al.* [9] includes the terms in the two first lines of this equation where Γ_n^{RG} and Γ_n^{RL} are the resonant capture and loss rates. The (empirical) statistical factor $w_n^{\mathrm{fin}}=1/(1+1.5a_n)$ corrects for the decrease in Auger transition rates $\Gamma_{n',n}^{\mathrm{AI}}$ due to increasing populations a_n of the final shell. As in Ref. [9], we only include the fastest Auger processes with equivalent active electrons in the initial state [23] for the relaxation of outer shells. The statistical factor $w_n^{\mathrm{ini}}=\frac{1}{2}a_n(a_n-1)$ takes the equivalence of electrons in the initial shell into account. The degeneracy of shell n is given by $A_n=2n^2$. Hydrogenic subshells are not resolved. θ is the unit step function and $\delta_{n,n'}$ the Kronecker symbol. For the present investigation, we have added the terms in the third and fourth line. The rates Γ_n^{SF}, Γ_n^{PO}, $\Gamma_{n',n}^{\mathrm{AI}}$, $\Gamma_n^{KLV_W}$, Γ^{CK}, Γ^{sCK}, and Γ^{KLM} account for SF, PO, AI, KLV_W, LLM-CK, LLL-sCK, and KLM processes.

G. Projectile motion

With respect to our previous work [23], we have refined the potential that governs the classical motion of the projectile. We replaced the planar averaged Thomas-Fermi-Molière (TFM) potential which satisfactorily describes grazing incidence collisions under surface channeling conditions [60] by the sum over binary TFM potentials for the interaction of the projectile with individual surface atoms. Recoil effects in close encounters with individual target atoms are included by switching to a binary collision mode at distances below one-half of a lattice constant [16]. The kinematics is first calculated in the center-of-mass system in terms of the reduced mass and a vector keeping track of the internuclear distance of the MCI and the target atom, and is later translated back into the laboratory system. Doing so, we assume the target atom to be unbound and at rest at its lattice site. The inclusion of target recoil leads to a closer approach of the projectiles to the first bulk layer as compared to a rigid crystal. It allows us to cover a larger range of incident angles and permits a more detailed description of the crystal surface orientation.

The projectile consequently moves according to Newton's equation

$$\Delta\vec{v}=\frac{\vec{F}(q,\vec{R})}{m_{\mathrm{nuc}}}\Delta t,\tag{11}$$

where the force

$$\vec{F}(q,\vec{R})=-\left(\frac{q(R)}{2(R-z_{\mathrm{im}})}\right)^2\hat{e}_z+\vec{F}_{\mathrm{TFM}}(\vec{R})\tag{12}$$

is composed of the self-induced image force and the TFM force including the kinematic recoil effect. Due to the dependence on the net projectile charge $q=q_{\mathrm{nuc}}-\Sigma_n a_n$, the projectile motion is coupled to its occupation evolution $\{a_n(t)\}$. Mass and charge of the projectile nucleus are designated as m_{nuc} and q_{nuc}.

H. Monte Carlo sampling

The use of atomic structure calculations within our simulation requires that the continuous charge current of the original COM [9,23] is related to transitions of electrons (charge discretization). The time integration over the multidimensional parameter space composed of the integer level occupations $\{a_n(t)\}$, the projectile trajectory $\vec{R}(t)$, and the locations of the surface atoms [cf. Eqs. (10) and (11)] is done based on random walks for an ensemble of 5000 incident particles. Starting at a random position shortly above the $(R=R_{\mathrm{crit}})$ plane, the MCI propagates with finite time steps Δt_i from one point in time t_i to the next t_{i+1} along its trajectory.

At each time t_i, separate values Δt_i for each transition type $X \in \{\mathrm{AI,RC,RL,SF,PO}\}$ are drawn from a negative exponential random number distribution

$$\Xi(\Delta t) = \left(\int_0^\infty \exp(-\Gamma^X \tau) d\tau \right)^{-1} \exp(-\Gamma^X \Delta t) \quad (13)$$

with a mean value equal to the average decay time $1/\Gamma^X$. The physical process supplying the smallest Δt_i is chosen to take place, and all variable parameters, such as configuration energies and occupations, are updated according to the change in $\{a_n(t)\}$. The projectile, in an electronic configuration given by Eq. (10), is then moved from $\vec{R}(t_i)$ to $\vec{R}(t_{i+1})$ by the force in Eq. (12). Now the same procedure starts over again leading to time step t_{i+2}, etc. Our code limits Δt_i to a maximum value of 1 in order to avoid large numerical steps in the integration yielding $\vec{R}$. If the smallest Δt_i turns out to be greater than 1, the projectile is moved with $\Delta t_i = 1$ without letting any electronic process take place.

III. POPULATION EVOLUTION OF THE HOLLOW ATOM

Before comparing our simulation results with experimental data, we look at the evolution of nonobservable quantities during the MCI-surface interaction. This will greatly assist us in the interpretation of the experimental data in Sec. IV. The Monte Carlo sampling as outlined in Sec. II H implies that one first of all has to define and keep track of physically meaningful event types. For each particle within the Monte Carlo sampling, a certain event, e.g., the ith resonant electron capture, may take place at different projectile locations $\vec{R}$ and may occur only for a small fraction of the particle runs. We stress that in this context the term statistical does not imply that the standard deviation $\sigma = \sqrt{(1/N)\Sigma_{k=1}^{N}(\xi_k - \overline{\xi})^2}$ attached to the simulated quantity ξ approaches zero if the number of particle runs N becomes very large. Instead, the error of the estimation for the width σ of the probability distribution converges to zero for $N \to \infty$. Due to its strong dependence on the particle history along the preceding trajectory, this distribution of simulated values ξ_k may significantly deviate from the Gaussian shape or even possess several maxima.

Accounting for the statistical interpretation, we display the corresponding results for each electronic transition/emission mechanism in three subplots. Figure 1 shows the resonant capture statistics for a N^{6+} beam and an Al(111) surface for an angle of incidence $\Theta = 45°$ and an incident kinetic energy $E_{\mathrm{kin}} = 80$ eV. This will also be our model system for the remaining plots in this section. The horizontal axis counts successive RC steps and acts as a (nonlinear) pseudotime axis to all three subplots.

The bottom plot describes the average fraction of particles for which the ith RC still takes place. Virtually the whole ensemble of MCI's resonantly captures twelve electrons. This curve can be fitted (with the relative error in the sum of squares below 0.001) to the function

$$f(i) = 50\,\mathrm{erfc}\left(\frac{i - \gamma_{\mathrm{RC}}}{\sqrt{2}\sigma} \right), \quad (14)$$

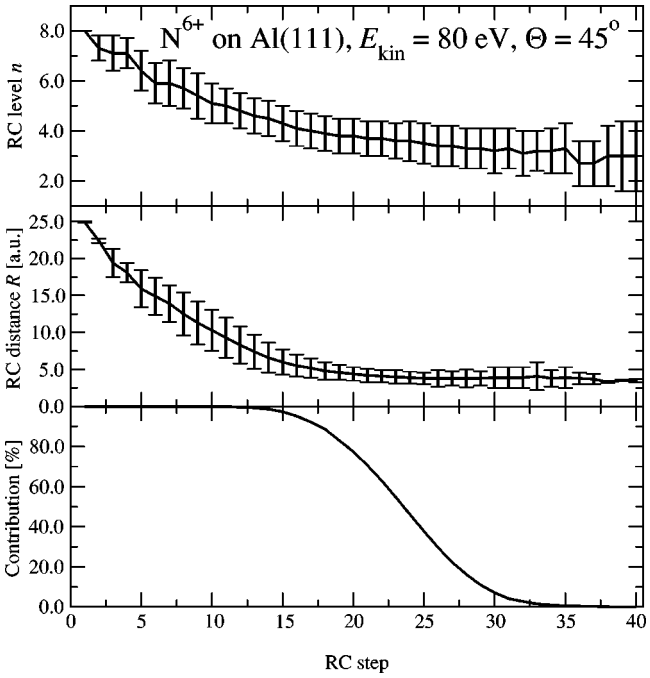

FIG. 1. Resonant-capture (RC) statistics for an ensemble of N^{6+} ions incident on an Al(111) surface under $\Theta = 45°$ with $E_{\mathrm{kin}} = 80$ eV. The horizontal axis applies to all upper graphs and marks successive RC events. From bottom to top, the three subplots display average values of the beam fraction undergoing the ith RC step, the corresponding distance from the first lattice layer R and atomic n shell involved, together with their statistical spread.

$$\mathrm{erfc}(x) = \frac{2}{\sqrt{\pi}} \int_x^\infty \exp(-\beta^2) d\beta,$$

with a standard deviation of $\sigma = 4.55$ from the mean value $\gamma_{\mathrm{RC}} = 23.0$. This means that the distribution is of Gaussian type, as expected for a large number of random number events. The small error in the fit shows that we have chosen a sufficiently large number of particle runs in the Monte Carlo sampling. For the following plots, we will only mention the value of the standard deviation σ for each event type.

The central plot in Fig. 1 shows the average location of the ith RC step and the error bars show their statistical spread σ. For all particles, the first capture distance R_{crit} lies in a tiny interval around 24.9 above the uppermost bulk layer. The simulated R_{crit} is in close agreement with the analytical formula $R_{\mathrm{crit}} = 1/2W\sqrt{8q+2} + z_{\mathrm{im}} = 25.8$ with the image plane located at $z_{\mathrm{im}} = 3.19$. On the average, about 10 RC steps take place in the remote interaction region where $R > 10$. Due to our restriction of RC to orbitals which do not fulfill the PO condition, RC events are limited to $R > 3.8$.

The upper plot in Fig. 1 illustrates which atomic shells are involved in the RC sequence. The first capture populates the $\overline{n} = \overline{n}_{\mathrm{crit}} = 8.0$ shell and successively proceeds to lower-lying shells. The sixth electron goes into the $\overline{n} = 5.9$ shell at $\overline{R} = 14.9$. RC seldom reaches shells with $n \leqslant 3$. This makes the accumulation of a significant L-shell population via RC highly unlikely.

The reverse electron transfer via RL is shown in Fig. 2. RL sets in at $\overline{R} = 16.2$ and mostly involves levels $4 \leqslant n \leqslant 8$.

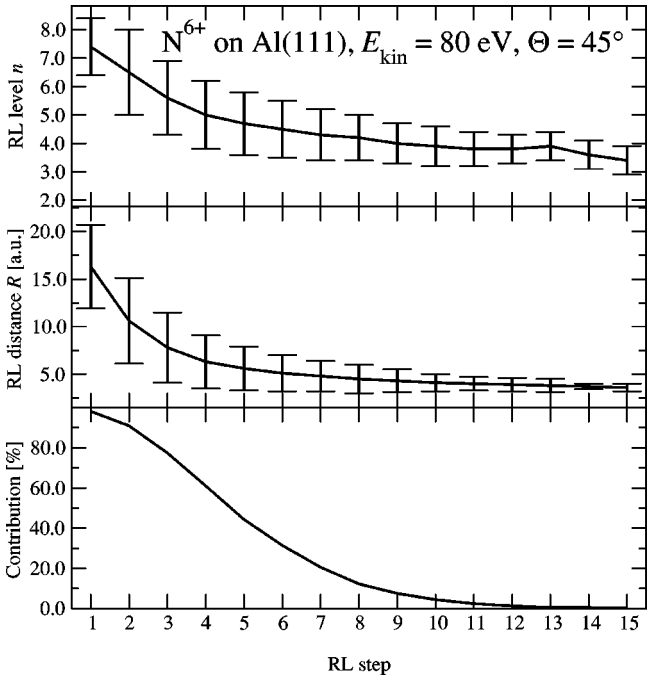

FIG. 2. Resonant-loss (RL) statistics for an ensemble of N^{6+} ions hitting an Al(111) surface under $\Theta = 45°$ and $E_{kin} = 80$ eV.

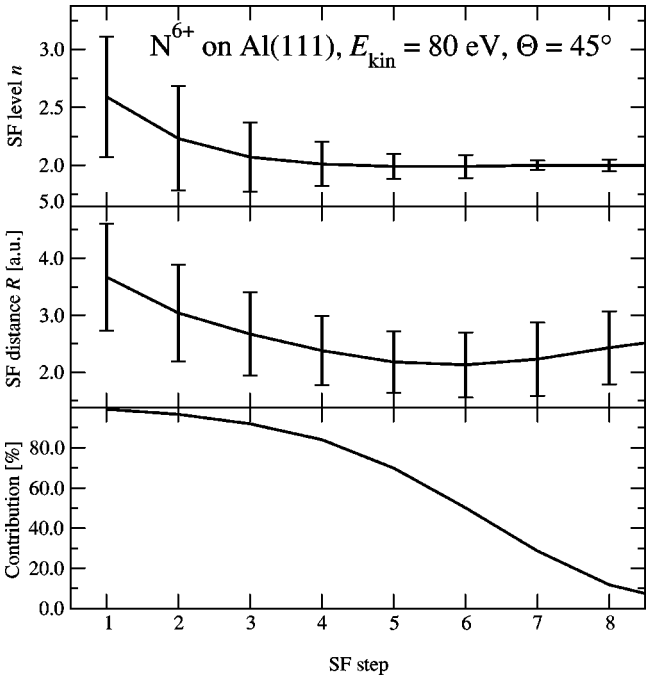

FIG. 4. Side-feeding (SF) statistics for an ensemble of N^{6+} ions hitting an Al(111) surface under $\Theta = 45°$ and $E_{kin} = 80$ eV.

On the average, only $\gamma_{RL} = 4.5 \pm 2.6$ electrons are lost to the target by RL while 23 electrons are passed from the valence band (VB) to the MCI by RC. The course of PO is displayed in Fig. 3. The onset of PO at $\overline{R} = 7.7$ from the $\overline{n} = 6.4$ level is located closer to the surface than the alternative RL loss channel. However, this process returns $\gamma_{PO} = 7.7 \pm 3.3$ electrons to the target. Contribution to PO are shells with $n = 4$, 5, and 6.

A similar above-surface scenario termed ''screening dynamics'' has been portrayed by Andrä *et al.* [26]. It was found that the interplay of resonant electron exchange and level shifts due to intra-atomic screening and image potentials leads to a partial relaxation of the MCI before bulk penetration. These ''screening dynamics'' are interrupted at $n \simeq 4$ when the level shift due the image potential and the mutual screening of the electrons fail to overcome the energy gap to the *M* shell. Resonant charge transfer is therefore cut off at this point. Due to the implementation of intra-atomic screening via Cowan code calculations in the EDCOM (cf. Sec. II A), this massive migration of electrons from n_{crit} into $n \simeq 4$, which is catalyzed by the metal surface, could be demonstrated in a dynamic simulation. In Sec. IV E 1, we will show that the KLV_W peak [43] is a characteristic signature of this phase.

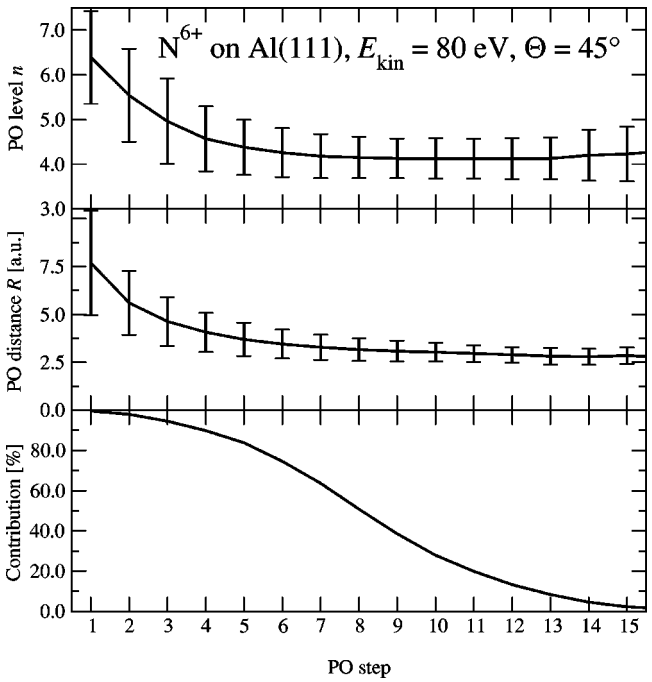

FIG. 3. Peel-off (PO) statistics for an ensemble of N^{6+} ions hitting an Al(111) surface under $\Theta = 45°$ and $E_{kin} = 80$ eV.

Side feeding from the induced charge cloud into still localized atomic levels is initiated when the overlap with the target electron distribution below the jellium edge (at z_j) becomes significant at average distances $\overline{R} = 3.7$ (Fig. 4). While approaching the high-electron density near the surface, the transfer switches from the *M* shell to the *L* shell, which is efficiently populated with $\gamma_{SF} = 5.4 \pm 1.9$ electrons. This phase embodies the transition from a very weak intra-atomic screening by the resonantly captured electrons towards the more efficient bulk screening when a tightly packed, induced charge cloud, resembling the *M* shell of an unperturbed atom, has formed. In Sec. IV E 1, the recently discovered foothill on the low-energy side of the KL_1L_1 Auger peak [43] will be associated with emission from this vacuum-bulk interface region.

With only $\gamma_{CP} = 1.3 \pm 1.2$ electrons reaching the continuum threshold after PO and RL have depleted outer projectile levels, continuum promotion (Fig. 5) plays a minor role in the electron loss. However, it is known that a large number of electrons $\gamma_{AI} \simeq q$ is ejected by the projectile via autoionization (AI) processes [15,61].

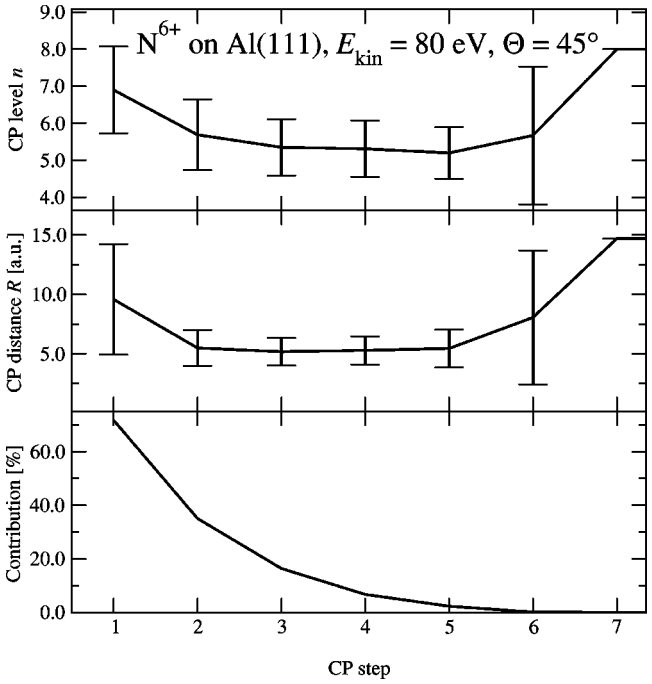

FIG. 5. Continuum-promotion (CP) statistics for an ensemble of N^{6+} ions hitting an Al(111) surface under $\Theta=45°$ and $E_{kin}=80$ eV.

Figure 6 gives details on the mean distance and the outermost level involved in the corresponding Auger transition (including CK, sCK, and KLV_W processes). The EDCOM predicts that a mean number of $\gamma_{AI}=8.8\pm2.9$ electrons are ejected by Auger emission. The charge balance from RC, RL, PO, SF, and CP amounts to a net transfer of 14.8 electrons towards the MCI. Subtracting γ_{AI}, it is found that $q=6$ electrons eventually stay with the MCI to attain a high degree of neutralization.

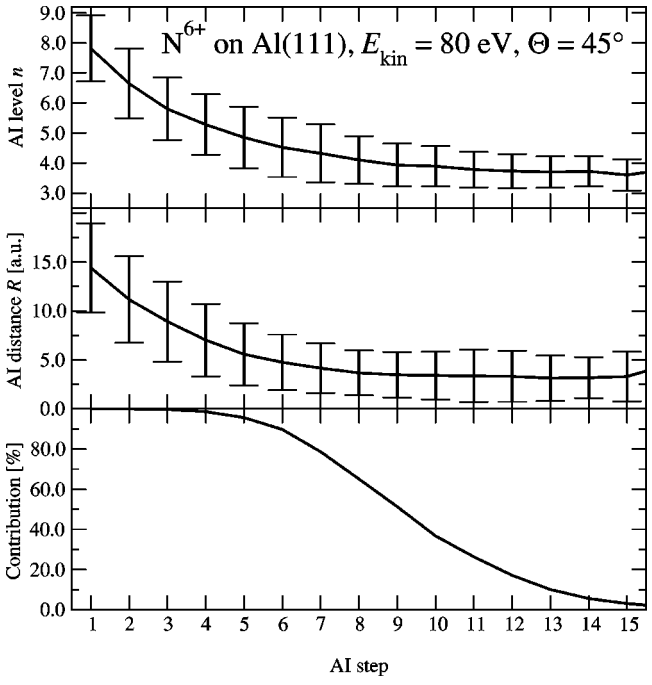

FIG. 6. Autoionization (AI) statistics for an ensemble of N^{6+} ions hitting an Al(111) surface under $\Theta=45°$ and $E_{kin}=80$ eV. The upper graph represents the outermost level, which is depleted by the corresponding Auger transition.

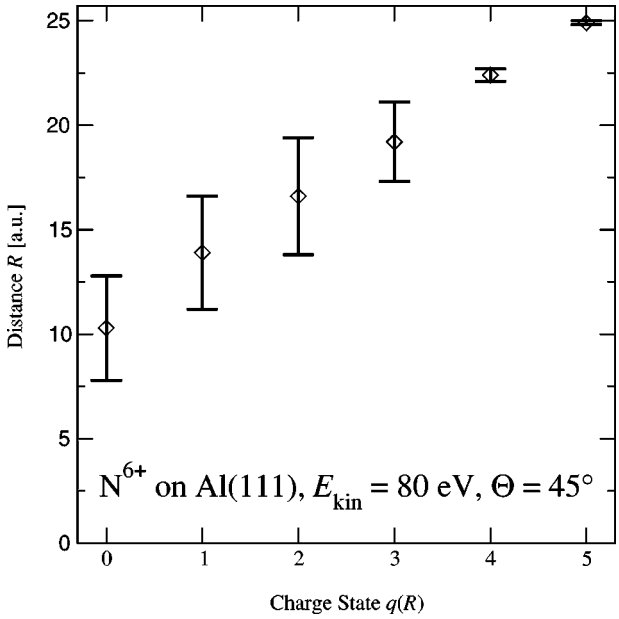

FIG. 7. Evolution of the projectile charge state q as a function of the ion-surface distance R for an ensemble of N^{6+} ions incident on an Al(111) surface under $\Theta=45°$ with $E_{kin}=80$ eV. The q-axis labels denote the ''new'' charge at distance R, e.g., the first capture changes q from 6 to 5 at $R=24.9$.

Due to the late onset of the loss mechanisms and the effective replenishment of atomic levels via RC and SF, the projectile is neutralized between R_{crit} and the tenth RC step at $\overline{R}=10.3$ (Fig. 7). It basically stays neutral or only singly charged at smaller distances to the surface. For $E_{kin}=80$ eV, 99.5% of the projectiles bounce back from the surface at a distance of $R_{min}=0.9$ from the first bulk layer according to our Thomas-Fermi-Molière modeling of the surface potential. Reducing E_{kin} to 10 eV while keeping $\Theta=45°$, the vertex moves away from the bulk to $R_{min}=2.0$.

IV. COMPARISON WITH MEASUREMENTS

In this section we employ the EDCOM to simulate various experimentally observable quantities within a single, fixed set of model parameters for all projectile and target species and conditions of incidence. Due to our simplifying approach, perfect agreement with the measurements cannot be expected, especially for quantities like the K-Auger electron spectra, which quite sensitively depend on a set of transition rates which are only known as rough estimates. Nevertheless, our simulation results will demonstrate reasonable agreement with all relevant experiments and reveal valuable information about the above-surface interaction dynamics.

A. Energy gains

For projectile charges $1<q<25$, the projectile kinetic energy gain due to its image charge attraction was observed to agree with the traditional COM formula $E_{gain}=Wq^{3/2}/(3\sqrt{2})$ [9,23,41,61], where W is the target work function. For high charge states $q>25$, energy gains falling

TABLE I. Comparison of projectile energy gains (divided by the substrate work function W) resulting from the COM formula $E_{\text{gain}}/W = q^{3/2}/3\sqrt{2}$ and our simulation results (right column) for hydrogenlike and metastable heliumlike second-row ions in configuration $(1s2s)$ at $E_{\text{kin}} = 100$ eV and $\Theta = 45°$. $v_\perp$ is the asymptotic projectile velocity component perpendicular to the surface.

			Energy gain/W	
			COM prediction:	Present simulation:
MCl	Target	$v_\perp$ (10^{-2} a.u.)	$\frac{q^{3/2}}{3\sqrt{2}}$	$\frac{E_{\text{gain}}}{W}$
C^{4+}	Al(111)	0.12	1.9	1.9
	Si(100)	0.12		2.1
C^{5+}	Al(111)	0.13	2.6	2.9
N^{5+}	Al(111)	0.12		3.0
		0.13		4.1
N^{6+}	Al(111)	0.38		3.8
		1.00	3.5	4.0
O^{6+}	Al(111)	0.13		3.9
	Si(100)	0.12		4.0
O^{7+}	Al(111)	0.13	4.4	5.5

short of the $q^{3/2}$ scaling have been observed [11,41] and attributed to intra-atomic screening effects [12]. We refer to the term energy gain as the kinetic energy gain of the projectile on its way towards the surface, resulting from the interplay of all forces acting on the projectile. For metals, these forces are given by the long-range self-image potential and the short-range surface potential [23].

We have confirmed that energy gains obtained with our improved simulation still agree with the commonly accepted COM results and experiments [23]. Regarding the significant modifications to our original code, this agreement cannot necessarily be expected. However, it is facilitated by the fact that the kinetic energy gain is mainly accumulated at large ion-surface separations, whereas the modifications discussed in this paper focus on close interactions. Table I lists energy gains according to the traditional COM formula and our new simulation output for hydrogenlike as well as metastable heliumlike projectiles. It can be seen that all values are in the vicinity of the traditional COM predictions and coincide with various experiments [11,41,61].

B. Final charge-state distributions

For slow highly charged ion beams scattering off surfaces, high fractions of completely neutralized projectiles, typically well above 90%, have been observed after reflection, even on insulating targets [11,55,56]. The remaining fraction overwhelmingly consists of singly charged positive and negative ions. As far as we know, no measured final projectile charge-state distributions $\{q_{\text{final}}\}$ are available for the incident energy regime below 100 eV. However, the measured high-energy Auger spectra in Sec. IV D will show that even for very slow projectiles (very small $v_\perp$) electron emission occurs predominantly out of neutral, mostly relaxed configurations.

In view of this lack of data, we compare our simulation output with measurements of other collision systems. It is important to stress that the traditional COM [9], applied to the full reflected trajectory of the ion, would lead to large fractions of ionized particles far after reflection in obvious contradiction to the experiment. Burgdörfer *et al.* [44] have included a resonant L-shell filling mechanism to comply with measured final charge states. Our study aims to reproduce the strong trend towards neutrality in the q_{final} distribution while, in addition, keeping agreement with other observables.

In Fig. 8 we plot the simulated charge fractions for $0 \leqslant q_{\text{final}} \leqslant 2$ in the final charge-state distributions for ground-state (gs) H-like ions and metastable (mt) He-like second row ions C^{q+}, N^{q+}, and O^{q+} in $(1s2s)$ configurations, impinging with $E_{\text{kin}} = 13q$ eV and a grazing angle of $\Theta = 5°$ on Al(111). The simulated fractions are recorded for reflected projectiles which have passed the first capture distance R_{crit}. After this point, less than 0.1% of the beam still exhibits the original K-shell vacancy, which eventually causes reionization. The remaining widely relaxed configurations lie below the autoionization threshold and may deexcite only via radiative processes without further electron emission.

Also shown is the measurement by Folkerts *et al.* [55] for O^{q+} $(3 \leqslant q \leqslant 8)$ at $E_{\text{kin}} = 3.75$ keV/amu on Au(110) under surface channeling conditions. Note that the simulation deals with different projectile types containing a single K-shell hole while the experiment refers only to O^{q+} projectiles with K-shell vacancies for $q \geqslant 7$. Running our code for projectiles possessing a filled K shell leads to slightly higher degrees of neutralization. Our Monte Carlo evaluation of the $q_{\text{final}} = 2$ fraction has a statistical error of about 40% while the $q_{\text{final}} = 1$ fraction is given within an error of 1.4%.

We observe that the experimental and simulated data agree well for the H-like ions. Shifting the final charge-state fractions of the metastables by $\Delta q = +1$ towards the right, the data points for the H-like and He-like counterparts roughly coincide with each other for $q_{\text{final}} \leqslant 1$ and also with the experiment. This means that the distribution of q_{final} mostly varies with the nuclear charge and is rather insensitive to the initial L electron. For all initial charge states q under consideration, the neutral contribution lies well above 90%. Under the assumption of a weak influence of the pro-

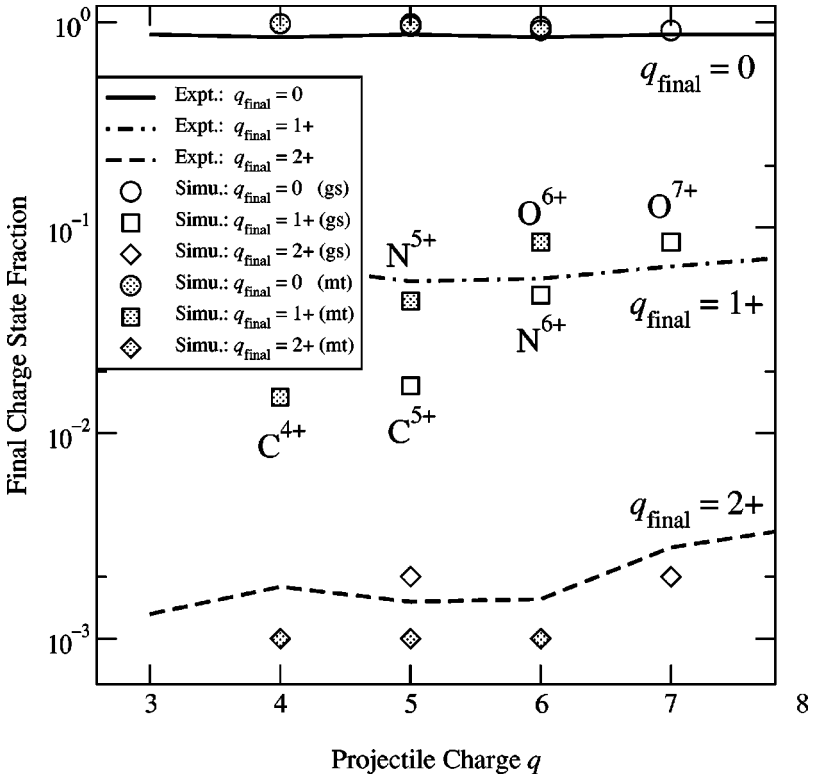

FIG. 8. Final charge-state fractions. The lines represent experimental data by Folkerts *et al.* [55] for O^{q+} impinging at $E_{kin}=3.75$ keV/amu on Au(110) under surface channeling conditions. The simulation results are given for H-like (*gs*) and He-like ($1s2s$) metastable (*mt*) C^{q+}, N^{q+}, and O^{q+} ions scattering with $E_{kin}=13q$ eV and $\Theta=5°$ off an Al(111) surface.

jectile kinetic energy, the measured charge-state distributions in Fig. 8 agree well with our simulation results.

C. Low-energy electron emission

Along the complicated interaction dynamics, electron emission originates from various sources. Apart from autoionization setting in as soon as more than two electrons have been captured, SF and CP contribute to the total electron yield. Other electron loss channels include PO, RL, and Auger emission into empty conduction-band states which do not contribute to measured electron yields.

In Fig. 9(a) we show experimental and simulated low-energy electron spectra for N^{6+} interacting with an Al(111) surface under $\Theta=45°$ for incident energies $E_{kin}=80$ and 10 eV. For these two systems, the image energy gains amount to $E_{gain}=17.1$ and 16.3 eV, respectively. The vanishing spectrometer transmission and stray magnetic fields aggravate the detection of electrons at the lowest displayed energies. Experience with our apparatus shows that the portion above $E>20$ eV is easily reproducible. The spectra in Fig. 9 and all the following plots are normalized to the integral *K*-Auger intensity. For the experimental data which have also been corrected by the spectrometer transmission, this is equivalent to a rescaling from emission into the acceptance solid angle of the spectrometer (0.031 sr) to emission into a full 4π sphere at a detection angle $\Psi=\Theta-90°$ with respect to the surface if a unity *K*-Auger yield and isotropic emission are assumed. The integral of the intensities over the energy axis therefore supplies the estimated total number γ of electrons per incident ion which are ejected into the vacuum. The simulated data have been convoluted with the spectrometer resolution of 0.7%.

For electron energies $E>10$ eV, the simulated spectra exhibit reasonable agreement with the experiment for both incident energies. One can recognize additional structures in the simulated spectra which are most likely caused by our simplified evaluation method of transition energies which considers only ground-state configurations for shells $n>2$ and neglects angular momentum coupling and the perturbation and hybridization of ionic levels near the surface [62,63]. Figure 9(b) displays the contributions of AI and SF to the simulated 80-eV spectrum. While the SF mechanism

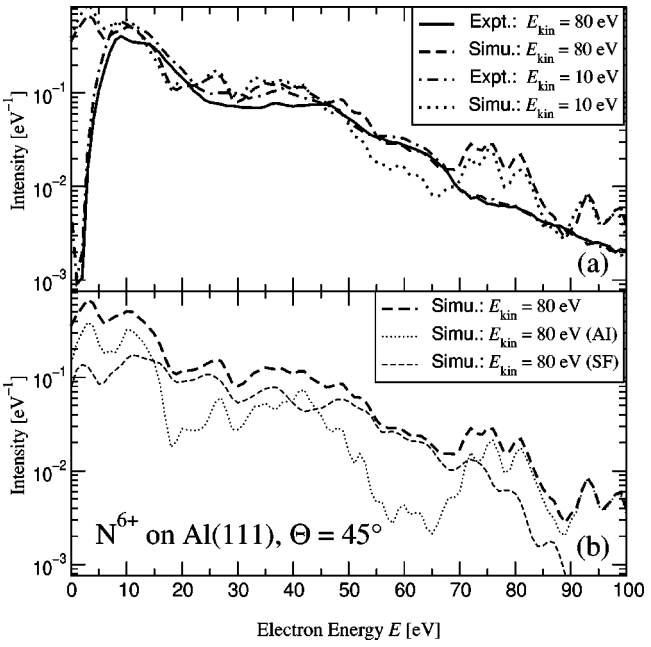

FIG. 9. Low-energy electron spectra of N^{6+} incident under $\Theta=45°$ on an Al(111) surface. Experimental and simulated spectra for incident energies $E_{kin}=80$ eV and 10 eV (a). Subplot (b) also shows SF and AI contributions to the $E_{kin}=80$ eV spectrum.

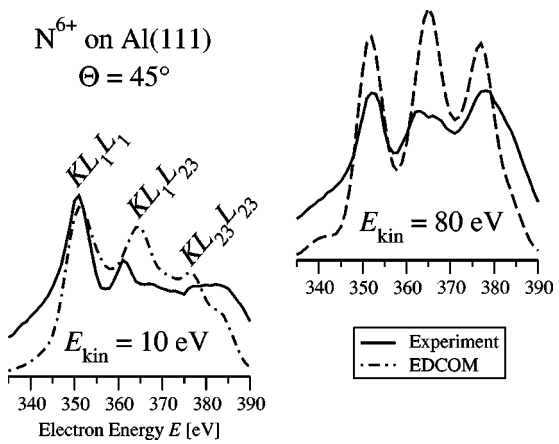

FIG. 10. *KLL* spectra of N^{6+} incident under $\Theta=45°$ on an Al(111) surface. Experimental and simulated spectra are displayed for the incident energies $E_{\mathrm{kin}}=10$ and 80 eV.

produces a comparatively smooth spectrum in the region $E<90\,\mathrm{eV}$, AI transitions generate structures below 20 eV, which we associate with the early stage of projectile relaxation above the surface when small Δn steps between Rydberg states prevail. In the same interaction phase, highly excited configurations may also emit *L*-Auger electrons which enhance the high-energy region. Integrating the spectral yields in Fig. 9 above 20 eV leads to yields of $\gamma=5.7$ and 5.8 emitted electrons per incident ion for the simulated spectra and to $\gamma=4.9$ and 4.3 for the experiments with $E_{\mathrm{kin}}=10$ and 80 eV, respectively.

Niemann *et al.* [15] have recently published low-energy Auger spectra for N^{6+} impinging on Au with E_{kin} ranging from 90 eV to 60 keV and perpendicular incidence. Integrating the total double-differential spectrum in energy and angle of detection to a full 4π solid angle, they observe total emission yields $\gamma=8.6\pm3.4$ for $E_{\mathrm{kin}}=90\,\mathrm{eV}$, which agrees well with their simulated yield of $\gamma_{\mathrm{AI}}=9.8$ for mere autoionization. With a different measurement technique, Eder *et al.* [64] measured a yield of $\gamma=9.8$ under similar scattering conditions.

For the same collision system, our EDCOM simulation including dynamic PO, CP, and SF mechanisms provides electron yields $\gamma_{\mathrm{AI}}=7.6$ for Auger emission (including the *K*-Auger electrons), $\gamma_{\mathrm{SF}}=6.6$ due to SF, and $\gamma_{\mathrm{CP}}=1.2$ due to CP. These values add up to a total yield $\gamma=15.4$ including contributions from $E<20\,\mathrm{eV}$. The discrepancy with Eder *et al.* and Niemann *et al.* might be rooted in the experimental difficulty to measure low-energy electrons ($E<20\,\mathrm{eV}$), which produce the greatest contribution to γ, as well as in the necessary simplifications embedded in our simulation.

D. *K*-Auger spectra of ground-state projectiles

K-Auger spectra for H-like and $(1s2s)$-metastable He-like incident ions can be subdivided into a well-structured *KLL* region, a broad, less intense peak consisting of *KLM* and *KLC* transitions, and small contributions from *KXY* transitions with $X,Y\in\{M,N,\ldots\}$. Figure 10 shows measured and simulated *KLL* electron spectra for N^{6+} colliding with an Al(111) surface under $\Theta=45°$ with $E_{\mathrm{kin}}=80\,\mathrm{eV}$ (upper right part) and $E_{\mathrm{kin}}=10\,\mathrm{eV}$ (lower left part). For both projectile energies, the *KLL* region extends between the KL_1L_1 peak at $E=352\,\mathrm{eV}$ and the $KL_{23}L_{23}$ peak at $E=378\,\mathrm{eV}$. The peak widths reflect the possibility of different initial *L*-shell populations n_L at the time of *K*-Auger decay. The broad *KLM*/*KLC* peak is situated on the high-energy side of the *KLL* region.

Figure 10 also displays the corresponding simulation results. In general, the *KLL* subpeak intensities sensitively depend on the ratio between the *L*-shell filling rate $\Gamma_L^{\mathrm{fill}}=\Gamma_{n,L}^{\mathrm{AI}}+\Gamma_L^{\mathrm{SF}}$ [given by Eqs. (1) and (6)] and *KLL* decay rates Γ_K^{AI}. We can give only crude estimates for Γ_n^{fill} in the relevant interaction region (cf. Sec. II D 1), and Γ_K^{AI} is known only for free ions [51,65] (cf. Sec. II A). For $n>2$, we have neglected the fine structure of the *n* shell in our simulation. The deviation on the low-energy end of the KL_1L_1 peak originates from an energy-loss background [30] in the experimental spectra which is not taken into account in the simulation. These considerations indicate that some deviations between simulation and experiment must be expected.

However, the changes in E_{kin} should affect the result in the same manner, i.e., the intensity ratios between different *KLL* subpeaks should shift similarly. Indeed, the EDCOM follows the experimental trend: towards increasing E_{kin}, the KL_1L_1 peak loses intensity, which is transferred into the upper part of the *KLL* spectrum. This can be understood in view of stronger side feeding into the $2p$ orbital when the vertex of the trajectory moves closer to the first lattice layer with increasing E_{kin} [16]. Near this turning point, the projectile is very slow and the exponentially decaying SF rates in Eq. (6) reach their maximum amplitude. The deviation in the peak region below 350 eV between the simulated and experimental difference spectra may be attributed to secondary effects such as the enhanced energy loss of the outgoing electrons with increasing E_{kin} [30,66] (not accounted for in our simulation).

The upper edge of the experimental $KL_{23}L_{23}$ peak is situated at a higher energy than in the simulation. In order to establish such a *KLL* energy, all six neutralizing electrons have to be present in the *L* shell. This might indicate that the SF rate Γ_n^{SF} in Eq. (6) which yields an average *L*-shell population $a_L=4.6$ at the time of *K*-Auger decay for $E_{\mathrm{kin}}=80\,\mathrm{eV}$ might be slightly underestimated. The *KLM*/*KLC* peak can be found around 401 eV (not shown). The simulation reproduces its position and enhancement for the lowest incident velocities more clearly than the experiment.

E. Auger spectra of metastable projectiles

In two recent publications [43,67], we discussed two characteristic signatures of the initial $2s$ electron in the *K*-Auger spectra of $(1s2s)$-metastable He-like C^{4+}, N^{5+}, and O^{6+} (and also Ne^{8+}) incident under $\Theta=5°$ with $E_{\mathrm{kin}}=13q$ eV on Al(111). The first feature is the tiny KLV_W peak on the upper side of the *KLM* region, which will be the subject of Sec. IV E 1. The second feature is a low-energy shoulder of the KL_1L_1 peak, which will be discussed in Sec. IV E 2.

1. The KLV_W peak

Guided by transition energy considerations, the KLV_W peak could be identified as an above-surface process involv-

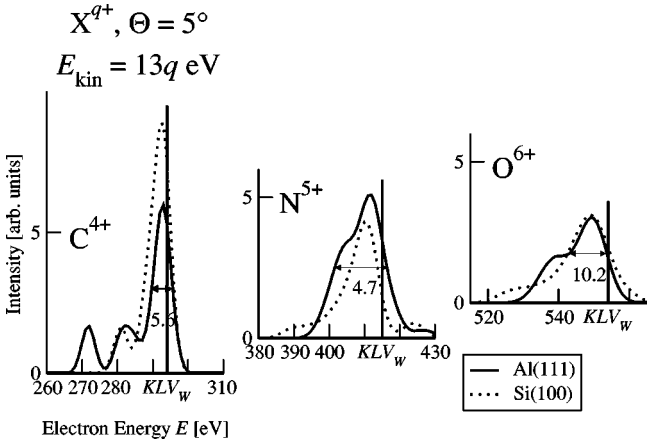

FIG. 11. KLV_W peak in the spectra of metastable, He-like MCI's impinging under $\Theta=5°$ and $E_{kin}=13q$ eV on Al(111) and Si(100). The vertical line marks the experimentally observed KLV_W peak position. The occurrence and transition energy of the KLV_W peak as well as the measured enhancement for the C^{4+}/Si(100) collision system and its broadening towards the O^{6+} projectile are qualitatively reproduced by the EDCOM simulation.

ing the K vacancy, the initial $2s$ electron, and an occupied atomic state (labeled ''V_W''), which is resonant with the target work function W, preferentially in the N or O shell. This finding is consistent with the strong dependence of the KLV_W rates on Δn in Eq. (2).

In Fig. 11, we display the EDCOM simulation of the partial KLV_W spectrum omitting all other K-Auger contributions. The simulation is carried out for an Al(111) and a Si(100) surface, primarily different in their work functions $W=4.25$ and 4.91 eV [68], respectively. The slightly deviating Fermi energies and lattice constants only have a minor impact on the simulation. Note also that the same scaling has been applied to energy and intensity axes of all three projectiles to illustrate the increasing KLV_W peak width from C^{4+} to O^{6+}, which coincides with the measurement [43]. This widening from about 6 eV (C^{4+}, N^{5+}) to about 10.2 eV (O^{6+}) can be explained by the quantum number of the initially populated projectile shell n_{crit}, which increases with q_{nuc}. This implies that electrons captured by O^{6+} need to descend more steps down the Auger-deexcitation ladder to the statistically preferred KLV_W configuration with $q_{nuc}-2$ electrons in the $n\simeq 4$ shell [43] than if they were captured by C^{4+}. This statistical spread of contributions to the KLV_W peak translates into an energy spread which is also amplified with increasing q_{nuc}.

The vertical line marks the experimentally observed KLV_W peak position, which is in all cases very close to the simulation output. We also find the suppression of the KLV_W peak in the spectra of H-like MCI's in the EDCOM (not shown). In [33,43] it was demonstrated that the KLV_W peak position is widely unaffected by switching from the Al(111) to the Si(100) target. However, the KLV_W peak appeared much stronger for C^{4+} projectiles on Si(100) as compared to Al(111) complying with the EDCOM results in Fig. 11. This can be understood by the greater work function W of Si(100) guiding RC into deeper-lying levels. Considering that the low q_{nuc} of C^{4+} implies an initial population of a mean shell $n_{crit}=5.6$ for Si (compared to $n_{crit}=6.0$ for Al), which is adjacent to the V_W level with $n_W=4$, subsequent KLV_W processes do not have to ''wait'' long for the accumulation of a sufficient population in the n_W shell. This effect disappears as higher-lying levels are resonantly populated with increasing q_{nuc}.

Proceeding from C^{4+} to O^{6+}, the EDCOM tells us that the KLV_W line is emitted at an average ion-surface distance moving from $R=9.6\pm 3.7$ down to 5.5 ± 2.7. This decrease is again correlated with the shell, which is populated by the first RC increasing from $n_{crit}=6$ to 8. Therefore, the population of the statistically preferred KLV_W levels with $n\leqslant 5$ takes longer. Note that the small increase of the initial charge q from 4 to 6 causes R_{crit} to grow from 21 to 25. However, the resulting prolonged above-surface interaction time $\Delta T_{crit}=\Delta R_{crit}/v_\perp \simeq 10^{-15}\,s^{-1}$ does not compensate for the additional steps on the relaxation, even when neglecting the increase of the image acceleration towards O^{6+}. Hence, the width of the KLV_W peak which is correlated with the fraction of KLV_W decays from $n_W=4$ increases towards O.

2. The KL_1L_1 foothill

In a recent publication [33], it was pointed out that a tiny foothill on the low-energy side of the KL_1L_1 peak is generated after KLV_W emission but prior to plunging into the jellium where most of the KLL transitions occur. It was argued that in this region SF into the L shell has already set in but is still too slow to provide more than one L electron. This explains the more pronounced appearance of the foothill in spectra of $(1s2s)$-metastable projectiles. The energy shift of this near-surface KL_1L_1 transition with respect to the main KL_1L_1 peak is caused by the induced electron cloud, which is more loosely packed than within the target electron gas. On the other hand, the presence of the screening cloud cuts off KLV_W emission. This is due to much faster KLL and KLM transitions and the fact that V_W levels are peeled off.

In Fig. 12 we distinguish between K-Auger emission from the remote ($R>5$), close ($z_j+1<R<5$), and ''subsurface'' ($R<z_j+1$) interaction region for $(1s2s)$-metastable incident O^{6+} ions. The plot confirms that the dominating contribution to the KLL foothill stems from the zone just above the jellium edge at $z_j=2.19$. Note that the vertex at $R_{min}=2.4$ is above the jellium edge. Therefore, the true subsurface contributions to the K-Auger spectrum remain comparatively small in this grazing incidence geometry where the ''subsurface'' region is restricted to $2.4<R<3.19$.

Figure 13 examines the occurrence of the foothill for the same projectiles as in Fig. 11. Similar to the KLV_W peak, the shoulder broadens from C^{4+} to O^{6+} on an absolute scale (note the differences in the E scaling in Fig. 13). As for the KLV_W peak, this effect can be related to the increase in q_{nuc} because the shift in the KL_1L_1 transition energies (due to the attenuated screening compared to the jellium region) is amplified by the effective nuclear charge. In summary, the proposed locations and order of the emission of the KLV_W peak and the KL_1L_1 foothill are confirmed by the EDCOM.

V. VARIATION OF MODEL PARAMETERS

In this section we study how the outcome of our simulation is affected by switching off or by changing the speed of

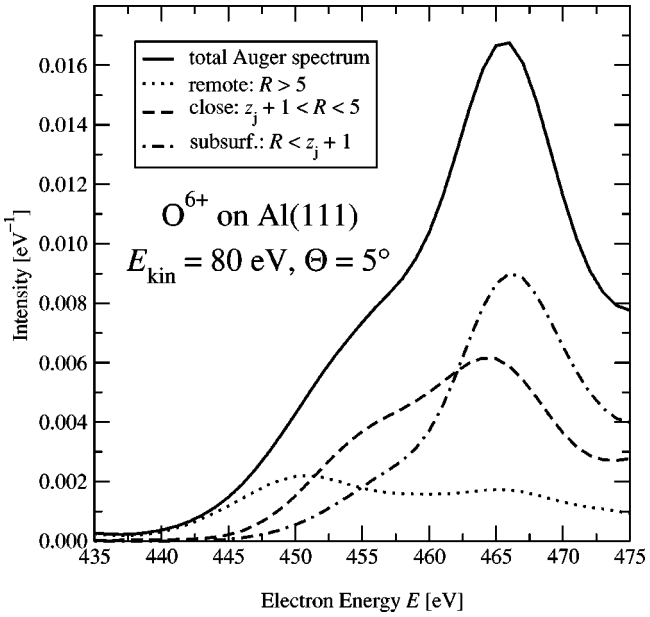

FIG. 12. KL_1L_1 foothill emission zones in the simulated spectra of metastable, He-like O^{6+} impinging under $E_{kin}=80$ eV and $\Theta=5°$ on Al(111). The solid line shows the total Auger spectrum. The three following lines represent the *K*-Auger spectrum emitted in the remote ($R>5$), close ($z_j+1<R<5$) and ''subsurface'' ($R<z_j+1$) interaction region.

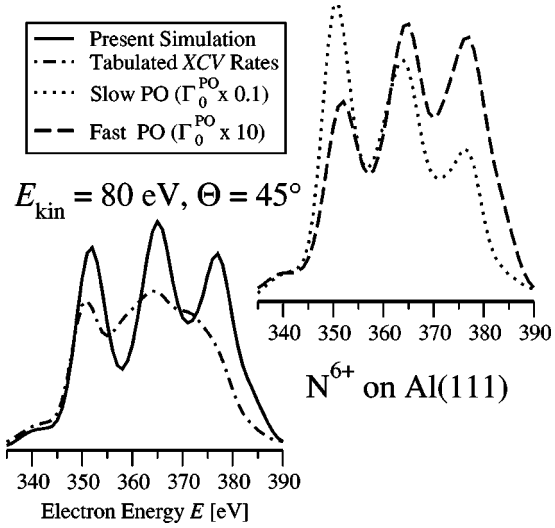

FIG. 14. Reshaping of the *KLL* region due to parameter variation for N^{6+} ions colliding with an Al(111) surface under $\Theta=45°$ and $E_{kin}=80$ eV. In the lower left plot, the implementation of the tabulated *XCV* rates [45] is compared to the present simulation. The upper right plot displays the *KLL* regions for rescaled PO base rates Γ_0^{PO}. By either fueling PO or SF, the $KL_{23}L_{23}$ intensity is clearly enhanced. Our choice of a unity scaling factor leads to the best agreement with the experimental structure.

certain interaction mechanisms for N^{6+} ions on Al(111). The modeling of interaction rates has been guided by semiclassical arguments. It has been justified by the consistent agreement of our simulation output with several observables for a variety of collision systems, which are characterized by E_{kin} and Θ as well as the projectile species and target type.

By completely disabling PO, electron loss is restricted to the less efficient RL and CP; see Figs. 2 and 3. After the projectile has been neutralized at $R\simeq 14.9$ (this is the same value as for the full simulation), most projectiles stay neutral unless they are reionized by the rather slow autoionization cascade. Since SF near the jellium edge is linked to a nonvanishing projectile charge that induces the VB electron cloud [cf. Eq. (6)], the filling of inner projectile levels is strongly suppressed.

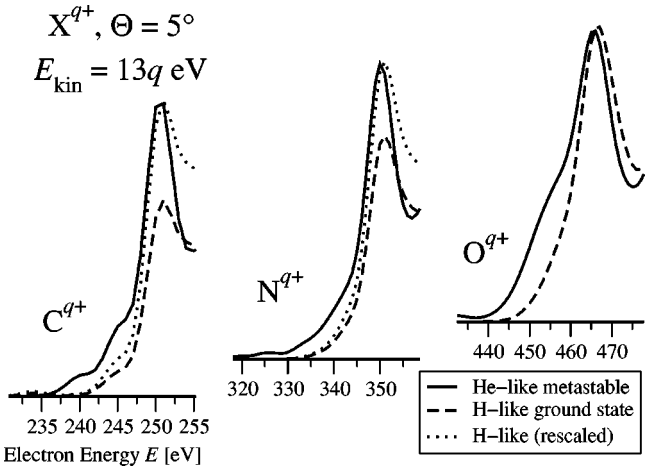

FIG. 13. KL_1L_1 foothill in the spectra of metastable, He-like MCI's impinging under $\Theta=5°$ and $E_{kin}=13q$ eV on Al(111) and Si(100). The occurrence of the KL_1L_1 shoulder in the spectra of all three He-like projectiles as well as the measured enhancement for its broadening towards the O^{6+} projectile are qualitatively reproduced by the simulation. The dotted line denotes the H-like ground-state spectrum, which is renormalized to the KL_1L_1 intensity of the metastable projectiles.

Thus, by disabling PO, we find that the *L* shell cannot be efficiently filled, in contrast to the high degree of *L*-shell filling at the moment of *KLL* decay observed in all experiments, e.g., in Ref. [33]. In addition, a high fraction of projectiles emerges from the target region still containing their initial *K* vacancy. This leads to a renewed ionization due to the pending *KLL* transition on the outgoing path. The simulation indeed shows that neglecting PO lets only 65.0% of the incoming ions emerge as neutrals in the asymptotic limit. The modified fraction of ionized projectiles would predict *KLL* energies in disagreement with experiment. Good agreement of the measured and simulated high-energy spectra and final projectile charge states thus appears to require the inclusion of PO.

Deactivating CP leaves the simulation output mostly unaffected. This can be understood by its minor impact on the electron transfer with an average number of 1.3 electrons lost to the continuum along the whole trajectory.

As mentioned before, SF is closely linked to PO because the charge content of the induced VB cloud matches the charge surplus of the projectile core [59]. By merely switching off SF, similar effects as for disabled PO can be observed. For instance, the fraction of particles which are ionized far after reflection increases to more than 50%. At the same time, the mean number of *L*-shell electrons at the time of *KLL* decay drops from 4.6 to 3.0. These changes lead to significant disagreement with measurements.

In Fig. 14, the reshaping of the *KLL* region following a variation of PO and SF rates is examined. The plot on the

lower left displays the simulation output taken from Fig. 10. It is compared to a simulation which implements the LCV rates for the N/Al system as listed in [45] instead of the SF rate in Eq. (6). These LCV rates seem to be too slow to account for a high degree of L-shell population at the time of KLL decay. The upper right part of Fig. 14 exhibits separate program runs with the peel-off rate Γ_n^{PO} given in Eq. (6) rescaled by factors of 0.1 and 10. A reduced Γ_n^{PO} leads to a similar effect as we have just seen for slowed down SF. Fast PO enhances the intensity on the side of the $KL_{23}L_{23}$ peak. As in the preceding paragraph, this behavior can be attributed to the interlaced operation of PO and SF, which strongly influences the population of the L shell. Note that the significant changes in the spectra of Fig. 14 are introduced by a small shift of the mean L population at the time of KLL decay of magnitude $\Delta n_L \simeq 0.5$.

VI. SUMMARY AND OUTLOOK

We have presented a semiclassical model for collisions of slow multiply charged ions with surfaces by Monte Carlo sampling along the entire ion trajectory. We incorporated electron peel off, side feeding, and continuum promotion in a dynamic manner. The evaluation of projectile energy levels has been based on atomic structure calculations. For the classical motion of the projectile we included all relevant binary interaction potentials between the projectile and individual surface atoms, thereby allowing for arbitrary angles of incidence.

Our results exhibit good agreement with various experimental observables for different combinations of projectiles, target types, incident angles, and beam energies. This has been achieved *without* adapting the code and the free parameters involved to a particular collision system. The occurrence of the KLV_W peak and the KLL foothill could be explained within the framework of a quantitative approach. Our simulations confirm the main aspects of a previously published interaction model [33].

The sensitivity of our results to the particular implementation of the added interaction mechanisms (SF,PO) has been studied by disabling them or varying their rates in separate program runs. It could be shown that the interplay between peel off and side feeding plays a vital role in the relaxation of the projectile and thus for the reproduction of experimental data. Many of the quantities which enter the simulation are known only approximately. For the future we intend to refine the modeling of rates and energies as presented in this work.

ACKNOWLEDGMENTS

This work was supported by the Division of Chemical Sciences, Office of Basic Energy Sciences, Office of Science, U.S. Department of Energy, by the National Science Foundation under Grant No. PHY-9604872, and by the DAAD.

[1] H. Ryufuku, K. Sasaki, and T. Watanabe, Phys. Rev. A **21**, 745 (1980).
[2] A. Niehaus, J. Phys. B **19**, 2925 (1986).
[3] A. Bárány, in *Proceedings of the XVI International Conference on the Physics of Electronic and Atomic Collisions*, edited by A. Dalgarno *et al.*, AIP Conf. Proc. No. 205 (AIP Press, New York, 1990), p. 246.
[4] A. Bárány and C. J. Setterlind, Nucl. Instrum. Methods Phys. Res. B **98**, 184 (1995).
[5] U. Thumm, J. Phys. B **27**, 3515 (1994); Comments At. Mol. Phys. **34**, 119 (1999).
[6] U. Thumm, A. Bárány, H. C. L. Hägg, and C. J. Setterlind, Phys. Rev. A **56**, 4799 (1997).
[7] U. Thumm, Phys. Rev. A **55**, 479 (1997).
[8] B. Walch, U. Thumm, M. Stöckli, C. L. Cocke, and S. Klawikowski, Phys. Rev. A **58**, 1261 (1998).
[9] J. Burgdörfer, P. Lerner, and F. W. Meyer, Phys. Rev. A **44**, 5674 (1991).
[10] J. Limburg, J. Das, S. Schippers, R. Hoekstra, and R. Morgenstern, Phys. Rev. Lett. **73**, 786 (1994).
[11] F. W. Meyer, L. Folkerts, H. O. Folkerts, and S. Schippers, Nucl. Instrum. Methods Phys. Res. B **98**, 441 (1995).
[12] C. Lemell, H. P. Winter, F. Aumayr, J. Burgdörfer, and F. Meyer, Phys. Rev. A **53**, 880 (1996).
[13] S. Hatke, A. Hoffknecht, S. Hustedt, J. Limburg, I. G. Hughes, R. Hoekstra, W. Heiland, and R. Morgenstern, Nucl. Instrum. Methods Phys. Res. B **115**, 165 (1996).
[14] N. Stolterfoht, D. Niemann, M. Grether, and A. Spieler, Nucl. Instrum. Methods Phys. Res. B **124**, 303 (1997).
[15] D. Niemann, M. Grether, A. Spieler, N. Stolterfoht, C. Lemell, F. Aumayr, and H. P. Winter, Phys. Rev. A **56**, 4774 (1997).
[16] J. Thomaschewski, J. Bleck-Neuhaus, M. Grether, A. Spieler, and N. Stolterfoht, Phys. Rev. A **57**, 3665 (1998).
[17] J. Limburg, S. Schippers, R. Hoekstra, R. Morgenstern, H. Kurz, M. Vana, F. Aumayr, and H. P. Winter, Nucl. Instrum. Methods Phys. Res. B **115**, 237 (1996).
[18] C. Auth, T. Hecht, T. Igel, and H. Winter, Phys. Rev. Lett. **74**, 5244 (1995).
[19] T. Neidhart, F. Pichler, F. Aumayr, H. P. Winter, M. Schmid, and P. Varga, Phys. Rev. Lett. **74**, 5280 (1995).
[20] F. W. Meyer, Q. Yan, P. A. Zeijlmans van Emmichoven, I. G. Hughes, and G. Spierings, Nucl. Instrum. Methods Phys. Res. B **125**, 138 (1997).
[21] M. Sporn, G. Libiseller, T. Neidhart, M. Schmid, F. Aumayr, H. P. Winter, P. Varga, M. Grether, D. Niemann, and N. Stolterfoht, Phys. Rev. Lett. **79**, 945 (1997).
[22] L. Hägg, C. O. Reinhold, and J. Burgdörfer, Phys. Rev. A **55**, 2097 (1997).
[23] J. Ducrée, F. Casali, and U. Thumm, Phys. Rev. A **57**, 338 (1998).
[24] H. Khemliche, T. Schlathölter, R. Hoekstra, R. Morgenstern, and S. Schippers, Phys. Rev. Lett. **81**, 1219 (1998).
[25] A. Arnau, F. Aumayr, P. M. Echenique, M. Grether, W. Heiland, J. Limburg, R. Morgenstern, P. Roncin, S. Schippers, R. Schuch, N. Stolterfoht, P. Varga, T. J. M. Zouros, and H. P. Winter, Surf. Sci. Rep. **27**, 113 (1997).
[26] H. J. Andrä, A. Simionovici, T. Lamy, A. Brenac, G. Lamboley, A. Pesnelle, S. Andriamonje, A. Fleury, M. Bonnefoy,

M. Chassevent, and J. J. Bonnet, in *Proceedings of the XVII International Conference on the Physics of Electronic and Atomic Collisions, Brisbane, 1991*, edited by W. R. MacGillivray, I. E. McCarthy, M. C. Standages, and A. Hilger (IOP, Bristol, UK, 1992), pp. 89–103.
[27] F. W. Meyer, S. H. Overbury, C. D. Havener, P. A. Zeijlmans van Emmichoven, and D. M. Zehner, Phys. Rev. Lett. **67**, 723 (1991).
[28] H. J. Andrä, A. Simionovici, T. Lamy, A. Brenac, and A. Pesnelle, Europhys. Lett. **23**, 361 (1993).
[29] J. Das and R. Morgenstern, Phys. Rev. A **47**, R755 (1993).
[30] R. Köhrbrück, M. Grether, A. Spieler, N. Stolterfoht, R. Page, A. Saal, and J. BleckNeuhaus, Phys. Rev. A **50**, 1429 (1994).
[31] J. Limburg, S. Schippers, I. Hughes, R. Hoekstra, R. Morgenstern, S. Hustedt, N. Hatke, and W. Heiland, Nucl. Instrum. Methods Phys. Res. B **98**, 436 (1995).
[32] J. Ducrée, R. Díez Muiño, J. Mrogenda, E. Reckels, M. Rüther, A. Heinen, C. Vitt, M. Venier, J. Leuker, and H. J. Andrä, Phys. Rev. A **57**, 1925 (1998).
[33] J. Ducrée, J. Mrogenda, E. Reckels, and H. J. Andrä, Nucl. Instrum. Methods Phys. Res. B **145**, 509 (1998).
[34] M. Schulz, C. L. Cocke, S. Hagmann, and M. Stöckli, Phys. Rev. A **44**, 1653 (1991).
[35] H. J. Andrä, A. Simionovici, T. Lamy, A. Brenac, G. Lamboley, S. Andriamonje, J. J. Bonnet, A. Fleury, M. Bonnefoy, M. Chassevent, and A. Pesnelle, Z. Phys. D **21**, Suppl. 135 (1991).
[36] J.-P. Briand, S. Thuriez, G. Giardino, G. Borsoni, V. L. Roux, M. Froment, M. Eddrief, C. de Villeneuve, B. D'Etat-Ban, and C. Sébenne, Phys. Rev. A **55**, R2523 (1997).
[37] J. P. Briand, D. Schneider, S. Bardin, H. Khemliche, J. Jin, Z. Xie, and M. Prior, Phys. Rev. A **55**, 3947 (1997).
[38] S. Winecki, C. L. Cocke, D. Fry, and M. P. Stöckli, Phys. Rev. A **53**, 4228 (1996).
[39] H. Khemliche, J. Limburg, R. Hoekstra, and R. Morgenstern, Nucl. Instrum. Methods Phys. Res. B **125**, 116 (1997).
[40] S. Winecki, M. P. Stöckli, and C. L. Cocke, Phys. Rev. A **55**, 4310 (1997).
[41] H. Winter, C. Auth, R. Schuch, and E. Beebe, Phys. Rev. Lett. **71**, 1939 (1993).
[42] C. Lemell, J. Stöckl, J. Burgdörfer, G. Betz, H. P. Winter, and F. Aumayr, Phys. Rev. Lett. **81**, 1965 (1998).
[43] J. Ducrée, J. Mrogenda, E. Reckels, M. Rüther, A. Heinen, C. Vitt, M. Venier, J. Leuker, and H. J. Andrä, Phys. Rev. A **58**, R1649 (1998).
[44] J. Burgdörfer, C. Reinhold, and F. Meyer, Nucl. Instrum. Methods Phys. Res. B **98**, 415 (1995).
[45] R. Díez Muiño, N. Stolterfoht, A. Arnau, A. Salin, and P. M. Echenique, Phys. Rev. Lett. **76**, 4636 (1996).
[46] A. Arnau, R. Köhrbrück, M. Grether, A. Spieler, and N. Stolterfoht, Phys. Rev. A **51**, R3399 (1995).
[47] N. V. Smith, C. T. Chen, and M. Weinert, Phys. Rev. B **40**, 7565 (1989).
[48] R. D. Cowan, *The Theory of Atomic Structure and Spectra* (University of California Press, Berkeley, 1981).
[49] N. Vaeck and J. E. Hansen, J. Phys. B **28**, 3523 (1995).
[50] H. J. Andrä, in *Physics of Highly-Ionised Atoms, Proceedings of the NATO Advanced Study Institute*, edited by R. Marrus (Plenum, New York, 1989).
[51] J. Hansen, O. Schraa, and N. Vaeck, Phys. Scr. **T41**, 41 (1992).
[52] L. Folkerts and R. Morgenstern, Europhys. Lett. **13**, 377 (1990).
[53] N. Stolterfoht, R. Köhrbrück, M. Grether, A. Spieler, A. Arnau, R. Page, A. Saal, J. Thomaschewski, and J. Bleck-Neuhaus, Nucl. Instrum. Methods Phys. Res. B **99**, 4 (1995).
[54] C. Lemell, H. P. Winter, F. Aumayr, J. Burgdörfer, and C. Reinhold, Nucl. Instrum. Methods Phys. Res. B **102**, 33 (1995).
[55] L. Folkerts, S. Schippers, D. M. Zehner, and F. W. Meyer, Phys. Rev. Lett. **74**, 2204 (1995); **75**, 983(E) (1995).
[56] S. Winecki, M. P. Stöckli, and C. L. Cocke, Phys. Rev. A **56**, 538 (1997).
[57] M. Grether, A. Spieler, R. Köhrbrück, and N. Stolterfoht, Phys. Rev. A **52**, 426 (1995).
[58] R. Díez Muiño, A. Arnau, and P. M. Echenique, Nucl. Instrum. Methods Phys. Res. B **98**, 420 (1995).
[59] R. Díez Muiño, A. Salin, N. Stolterfoht, A. Arnau, and P. M. Echenique, Phys. Rev. A **57**, 1126 (1998).
[60] D. S. Gemmell, Rev. Mod. Phys. **46**, 129 (1974).
[61] H. Kurz, F. Aumayr, H. P. Winter, D. Schneider, M. A. Briere, and J. W. McDonald, Phys. Rev. A **49**, 4693 (1994).
[62] P. Kürpick, U. Thumm, and U. Wille, Nucl. Instrum. Methods Phys. Res. B **125**, 273 (1997).
[63] P. Kürpick and U. Thumm, Phys. Rev. A **58**, 2174 (1998).
[64] H. Eder, M. Vana, F. Aumayr, H. P. Winter, J. I. Juaristi, and A. Arnau, Phys. Scr. **T73**, 322 (1997).
[65] S. Schippers, J. Limburg, J. Das, R. Hoekstra, and R. Morgenstern, Phys. Rev. A **50**, 540 (1994).
[66] J. Mrogenda, J. Ducrée, E. Reckels, J. Leuker, and H. J. Andrä, Appl. Surf. Sci. **136**, 269 (1998).
[67] J. Ducrée, J. Mrogenda, E. Reckels, and H. J. Andrä, in Proceedings of the IX International Conference on the Physics of Highly Charged Ions [Phys. Scr. (to be published)].
[68] N. W. Ashcroft and N. D. Mermin, *Solid State Physics* (Saunders, Philadelphia, 1976).